From global to local: exploring the relationship between parameters and behaviors in models of electrical excitability

Patrick Fletcher, Richard Bertram & Joel Tabak

Journal of Computational Neuroscience

ISSN 0929-5313
Volume 40
Number 3

J Comput Neurosci (2016) 40:331-345
DOI 10.1007/s10827-016-0600-1

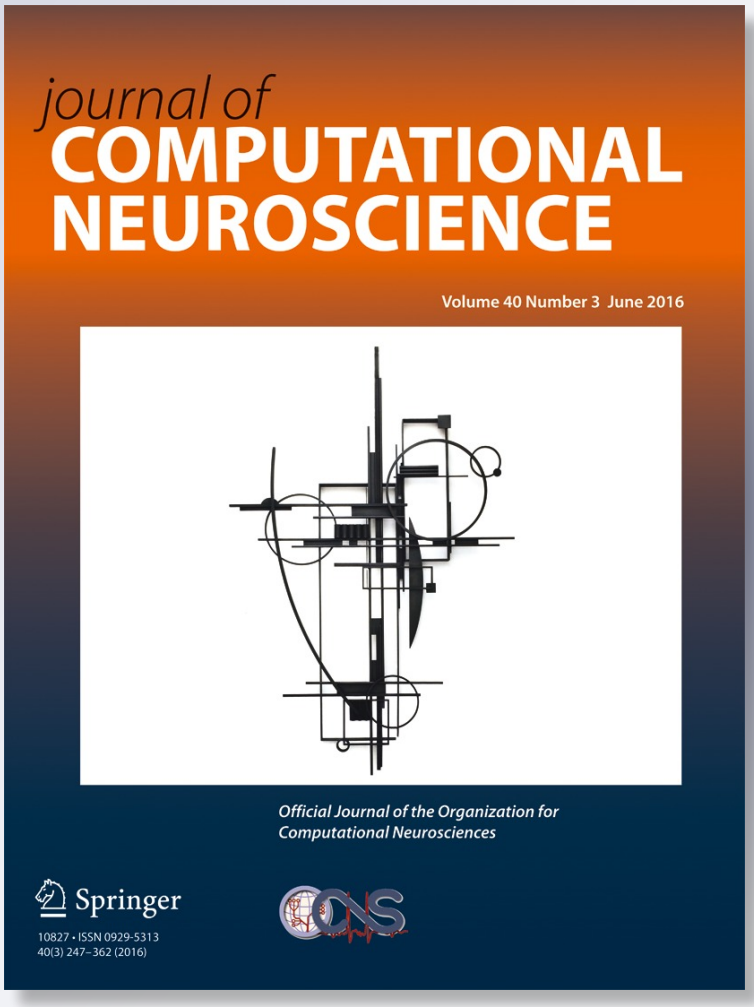

Springer

Your article is protected by copyright and all rights are held exclusively by Springer Science +Business Media New York. This e-offprint is for personal use only and shall not be self-archived in electronic repositories. If you wish to self-archive your article, please use the accepted manuscript version for posting on your own website. You may further deposit the accepted manuscript version in any repository, provided it is only made publicly available 12 months after official publication or later and provided acknowledgement is given to the original source of publication and a link is inserted to the published article on Springer's website. The link must be accompanied by the following text: "The final publication is available at link.springer.com".

Author's personal copy

J Comput Neurosci (2016) 40:331–345
DOI 10.1007/s10827-016-0600-1

From global to local: exploring the relationship between parameters and behaviors in models of electrical excitability

Patrick Fletcher[2] · Richard Bertram[1] · Joel Tabak[3]

Received: 30 October 2015 / Revised: 2 March 2016 / Accepted: 7 March 2016 / Published online: 1 April 2016
© Springer Science+Business Media New York 2016

Abstract Models of electrical activity in excitable cells involve nonlinear interactions between many ionic currents. Changing parameters in these models can produce a variety of activity patterns with sometimes unexpected effects. Furthermore, introducing new currents will have different effects depending on the initial parameter set. In this study we combined global sampling of parameter space and local analysis of representative parameter sets in a pituitary cell model to understand the effects of adding K^+ conductances, which mediate some effects of hormone action on these cells. Global sampling ensured that the effects of introducing K^+ conductances were captured across a wide variety of contexts of model parameters. For each type of K^+ conductance we determined the types of behavioral transition that it evoked. Some transitions were counterintuitive, and may have been missed without the use of global sampling. In general, the wide range of transitions that occurred when the same current was applied to the model cell at different locations in parameter space highlight the challenge of making accurate model predictions in light of cell-to-cell heterogeneity. Finally, we used bifurcation analysis and fast/slow analysis to investigate *why* specific transitions occur in representative individual models. This approach relies on the use of a graphics processing unit (GPU) to quickly map parameter space to model behavior and identify parameter sets for further analysis. Acceleration with modern low-cost GPUs is particularly well suited to exploring the moderate-sized (5-20) parameter spaces of excitable cell and signaling models.

Keywords Electrical activity · Pituitary lactotroph · Global parameter sampling · Bifurcation analysis · Graphics processing unit

1 Introduction

Many biological phenomena, such as cell electrical activity or chemical reaction networks, are studied using coupled systems of nonlinear ordinary differential equations (ODEs). These may produce solutions with rich dynamics, including equilibria, limit cycles, as well as the possibility of coexistence of multiple stable solutions for a given set of parameters. Multi-scale oscillations can also occur, such as chaotic trajectories or bursting oscillations, which consist of periodic episodes of fast oscillations or spikes. A key task in developing and analyzing such models is to understand how parameters of the model affect features of its solutions, such as the period and amplitude of an oscillation, or the number of spikes per burst. In particular, it is of interest to understand how the role of a parameter depends on the context of all the other parameters in the model. Attaining a

Action Editor: Bard Ermentrout

✉ Richard Bertram
bertram@math.fsu.edu

[1] Department of Mathematics, Florida State University, Tallahassee, FL 32306, USA

[2] Currently at the Laboratory of Biological Modeling, National Institutes of Health, Bethesda, MD 20892, USA

[3] Currently at the University of Exeter Medical School, Biomedical Neuroscience Research Group, EX4 4PS, Exeter, UK

Author's personal copy

global understanding of the relationship between parameter space and feature space can be challenging even for a modest number of parameters, owing to the nonlinear nature of such models.

The relationship between model parameters and solution features has been explored using both local and global approaches. "Local" methods provide information about solutions near a given point in parameter space or in a low-dimensional subspace of the whole parameter space. The most basic of these approaches is hand-tuning of parameters using direct numerical simulation, whereby parameters are manually adjusted to see their effect on solutions (Sherman 2011). This approach relies on (and builds) the modeler's intuition for how individual parameters affect the features of the solution. Typically this exploration in parameter space involves only a few parameters at a time, as one will begin with a specific point in parameter space and make incremental parameter changes from there. This process can be automated using brute force parameter sweeps, where features of model behavior (such as spikes per burst) are computed across two-dimensional parameter subspaces and then visualized to guide further mathematical analysis (Storace et al. 2008; Barrio and Shilnikov 2011; Linaro et al. 2012; Barrio et al. 2015).

Numerical continuation is another method used to discover the behavior of model solutions over a range of parameter values (Sherman 2011). Commonly used implementations are due to Doedel and Kernevez (1986) and Dhooge et al. (2003). Once a solution of interest is found, typically an equilibrium point or a periodic orbit, continuation tracks the solution as a few parameters change (usually one or two). In addition to tracking generic solutions, continuation is able to track the bifurcation points of these solutions, such as Hopf bifurcation points. The result is a bifurcation diagram: a graph indicating the tracked solutions (and their stability), separated by bifurcation points. This approach can be used to extend and organize the process of hand tuning and 2 or 3-dimensional brute force parameter sweeps, and is useful for summarizing model behavior for a small number of parameters at a time (Sherman 2011). Due to the low-dimensional nature of hand-tuning and numerical continuation, the computations required are completed rapidly on modern desktop computers. This means such computations are "disposable;" that is, one can test new ideas and follow intuition with little delay due to computation time. While these local methods provide excellent tools for exploring and explaining the relationship between parameters and solutions for a few parameters at a time, they become cumbersome as the dimension of parameter space is increased.

Other methods are more "global" in that they attempt to gain an understanding of solutions across a higher-dimensional subspace of parameter space. These include global sensitivity analysis methods (Iooss and Lemaître 2015), and brute force model database techniques (Günay 2014) which attempt to systematically sample a large number of independent parameter combinations throughout a large subset of (or the entirety of) the model's parameter space. Model databases have been developed to study crustacean stomatogastric ganglion (STG) neurons and networks (Goldman et al. 2001; Prinz et al. 2003, 2004; Taylor et al. 2009; Kispersky et al. 2012; Caplan et al. 2014), the escape swim network of the mollusk *Tritonea diomedea* (Calin-Jageman et al. 2007), the rat globus pallidus neuron (Günay et al. 2008), rat pituitary lactotroph cells (Tabak et al. 2011), the leech heart half-center oscillator (Doloc-Mihu and Calabrese 2011), and the lobster cardiac ganglion (Williams et al. 2013). In the database approach, at each of the many sampled points in parameter space, the solution (or features of the solution) is computed and the results are stored for later analysis. This offers the benefit of a more global perspective across a higher-dimensional parameter space. Particularly, one can ask whether the change in a model behavior due to a change in parameters is generic, or whether it depends on the context of the values of all the other parameters in the system. One drawback of brute force approaches is the large computation time required to complete all the simulations, which means such studies are often run on computer clusters. Similarly, global sensitivity analysis can require a large, computationally intensive sampling of the desired parameter search space (Iooss and Lemaître 2015), particularly when the model responses involve the computation of solutions of nonlinear ODEs.

Modern programmable graphics processing units (GPUs) are powerful massively parallel processors well suited to the task of accelerating brute force parameter search computations. They are available on desktop workstations and laptop computers at a low cost. Indeed, GPUs are increasingly being used to accelerate numerical simulations in neuroscience-related contexts, such as central pattern generator neuronal networks (Rodríguez et al. 2015; Barrio et al. 2015), spiking neural network simulations (Brette and Goodman 2012), and simulation of the circadian pacemaker of the suprachiasmatic nucleus (DeWoskin et al. 2014).

In this study, we employ a GPU-accelerated model database technique to investigate how the properties of a model of pituitary cell electrical activity (Tabak et al. 2011) vary across a 5-dimensional parameter space. The model solutions mimic the electrical properties of endocrine cells such as pituitary lactotrophs, which can exhibit quiesent, spiking, and bursting behaviors. The type of pattern produced is physiologically important, since hormone secretion from the cells is triggered by the influx of Ca^{2+} ions associ-

Author's personal copy

ated with that pattern of electrical activity (Van Goor et al. 2001). These activity patterns are known to change when cells are exposed to hormones, and these changes are in many cases due to increases in the conductances of K^+ ion channels (Stojilković et al. 2010). Because these conductances may affect electrical activity in different ways depending on the context defined by the expression of other conductances, we first generate a database of models with widely varying parameter values. Based on these different contexts, we examine how changes in the conductances of three different types of K^+ channels influence the behavior of the entire population of models. The model database approach allows the study of "macroscopic" changes in subpopulations models exhibiting specific behaviors (such as quiescence, spiking, and bursting), as well as the "microscopic" transitions that each individual model undergoes. These changes are then studied in representative models using bifurcation analysis and fast/slow analysis (Rinzel and Ermentrout 1998) to understand the underlying mechanism. Thus, the global database analysis technique is combined with local analysis to first see *what happens* and then to understand *why it happens*.

The use of the GPU greatly facilitates the sampling of parameter space, allowing it to be performed in a few seconds. This means brute force parameter sweeps and model database computations can share the benefit of being "disposable" computations. Analysis is also facilitated by algorithms that extract *features* of the activity time courses as they are being computed. The dependency of the activity features (such as amplitude, burst duration, or number of spikes per burst) on parameters can then be readily displayed. This global inspection of behaviors makes it easy and quick to identify general biologically relevant trends, such as the propensity of a certain type of ion channel to produce bursting. Global sampling of parameter space also has the potential to identify interesting and perhaps unexpected transitions between activity patterns that motivate further investigation with tools such as fast/slow analysis. This combined global/local approach has great applicability in model exploration and analysis.

2 Methods

2.1 Model description

The model is based on a previously described lactotroph model (Tabak et al. 2011). We consider a base model that includes a voltage-gated Ca^{2+} current (I_{Ca}), a delayed rectifier K^+ current (I_K), a Ca^{2+}-activated K^+ current (I_{SK}), and a leak current (I_L). The model includes three variables, membrane potential (V), activation of I_K (n), and the intracellular Ca^{2+} concentration (c), governed by the following equations:

$$C_m \frac{dV}{dt} = -(I_{Ca} + I_K + I_{SK} + I_L), \quad (1)$$

$$\tau_n \frac{dn}{dt} = n_\infty(V) - n, \quad (2)$$

$$\frac{dc}{dt} = -f_c(\alpha I_{Ca} + k_c c). \quad (3)$$

We then study the effects of increasing one of three additional currents: an inward rectifying K^+ current (I_{Kir}), a BK-type K^+ current (I_{BK}), and an A-type K^+ current (I_A). BK channels are both Ca^{2+} and voltage activated. We choose to model a subpopulation of BK channels closely associated with Ca^{2+} channels. In a small region near the opening of a Ca^{2+} channel, the $[Ca^{2+}]$ varies rapidly and its dynamics closely follow the dynamics of the membrane potential. We therefore approximate I_{BK} activation as voltage dependent (Fakler and Adelman 2008; Sherman et al. 1990). These additional currents add terms to the voltage equation:

$$C_m \frac{dV}{dt} = -(I_{Ca} + I_K + I_{SK} + I_{Kir} + I_{BK} + I_A + I_L). \quad (4)$$

Two equations for the gating variables associated with inactivation of I_A (h) and activation of I_{BK} (b) are also added to the system (1–3):

$$\tau_{BK} \frac{db}{dt} = b_\infty(V) - b, \quad (5)$$

$$\tau_h \frac{dh}{dt} = h_\infty(V) - h. \quad (6)$$

The ionic currents are given by:

$$I_{Ca} = g_{Ca} m_\infty(V)(V - E_{Ca}) \quad (7)$$

$$I_K = g_K n(V - E_K) \quad (8)$$

$$I_{SK} = g_{SK} s_\infty(c)(V - E_K) \quad (9)$$

$$I_{Kir} = g_{Kir} k_\infty(V)(V - E_K) \quad (10)$$

$$I_{BK} = g_{BK} b(V - E_K) \quad (11)$$

$$I_A = g_A a_\infty(V) h(V - E_K) \quad (12)$$

$$I_L = g_l(V - E_l) \quad (13)$$

with the steady-state activation functions

$$x_\infty(V) = [1 + \exp((V_x - V)/s_x)]^{-1} \quad (14)$$

$$s_\infty(c) = \frac{c^2}{c^2 + k_s^2} \quad (15)$$

where $x \in \{m, n, k, b, a, h\}$. Default parameter values listed in Table 1 give rise to a spiking activity pattern, when $g_{Kir} = g_A = g_{BK} = 0$. All simulations had the same initial condition: $V = -60$ mV, $n = 0.1$, $c = 0.1\mu M$, $b = 0.1$, and $h = 0.1$.

Author's personal copy

Table 1 Parameter values for the lactotroph model. Ranges are given in square brackets for parameters that were varied

Parameter	Value	Description
C_m	10 pF	Membrane capacitance
E_{Ca}	60 mV	Reversal potential for Ca^{2+} current
E_K	-75 mV	Reversal potential for K^+ current
E_L	-50 mV	Reversal potential for leak current
g_{Ca}	2 [0.5, 3.5] nS	Maximal Ca^{2+} channel conductance
V_m	-20 mV	Half-maximal voltage for m_∞
s_m	12 mV	Slope parameter for m_∞
g_K	3.2 [0.8, 5.6] nS	Maximal delayed rectifier K^+ channel conductance
V_n	-5 mV	Half-maximal voltage for n_∞
s_n	10 mV	Slope parameter for n_∞
τ_n	30 ms	Time constant for n
g_{SK}	2 [0.5, 3.5] nS	Maximal SK channel conductance
k_s	0.4 μM	Half-maximal Ca^{2+} for s_∞
g_{Kir}	0 [0, 2] nS	Maximal inward rectifier K^+ channel conductance
V_k	-65 mV	Half-maximal voltage for k_∞
s_k	-8 mV	Slope parameter for k_∞
g_{BK}	0 [0, 4] nS	Maximal BK channel conductance
V_b	-20 mV	Half-maximal voltage for b_∞
s_b	2 mV	Slope parameter for b_∞
τ_{BK}	5 ms	Time constant for b
g_A	0 [0, 100] nS	Maximal A-type channel conductance
V_a	-20 mV	Half-maximal voltage for a_∞
s_a	10 mV	Slope parameter for a_∞
V_h	-60 mV	Half-maximal voltage for h_∞
s_h	-5 mV	Slope parameter for h_∞
τ_h	20 ms	Time constant for h
g_L	0.2 [0.05, 0.35] nS	Maximal leak conductance
f_c	0.01	Fraction of free cytosolic Ca^{2+}
α	0.0015 μ M fC $^{-1}$	Conversion of charge to concentration
k_c	0.12 [0.03, 0.21] ms^{-1}	Rate of Ca^{2+} extrusion

2.2 Numerical methods

Parameter grids and model database computations were performed using custom OpenCL code running on nVidia graphics processing units. ODEs were numerically integrated using the Runge-Kutta fourth order method with a time step of 0.5 ms. Solution trajectories are not stored, but instead reduced to a set of *summary features* during the process of numerical integration. This greatly reduces the memory storage needs and allows a large number of simulations to be run in parallel on the GPU. Relevant points of the trajectory used to compute features are illustrated for a bursting trajectory in Fig. 1. The first 10 s of simulated time were discarded as transient behavior. In the following 40 s of simulation, the absolute maximum and minimum voltage ($\max V$, $\min V$; red downward and upward triangles, respectively, in Fig. 1) and voltage slope ($\max(dV/dt)$, $\min(dV/dt)$; blue rightward and leftward triangles, respectively, in Fig. 1) were recorded. From these special points in the time course, we determined if oscillations were present, and if so, computed event detection thresholds to be used in feature computation in the final 100 s of simulation.

If the amplitude ($\max V - \min V$) is larger than 10 mV, then oscillations are considered to be present. For oscillating solutions, we divided the trajectory into active and silent phases. An active phase begins when the voltage increases beyond the voltage threshold ($0.35 \cdot (\max V - \min V)$; red dashed line in Fig. 1) and the voltage slope increases beyond a positive slope threshold ($0.25 \cdot \max(dV/dt)$; upper blue dash-dotted line, Fig. 1 right panel). The beginning of an active phase is indicated in Fig. 1 by a black square. The active phase ends and the silent phase begins when the voltage drops below the voltage threshold and the voltage slope rises above the negative slope threshold ($0.25 \cdot \min(dV/dt)$; lower blue dash-dotted line, Fig. 1 right panel). This is indicated by a black circle in Fig. 1.

Author's personal copy

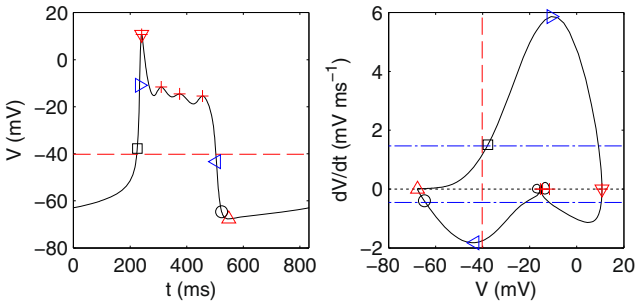

Fig. 1 Thresholds and salient points of trajectories used to compute solution features. One burst from the mean bursting model is shown as a timecourse (left panel, V vs t) and as a phase plot (right panel, dV/dt vs V), which shows the same burst trajectory as a loop traversed clockwise. The absolute maximum and minimum voltage (red downward and upward triangles, respectively) are used to compute a voltage threshold (red dashed line, $0.35 \cdot (\max V - \min V)$). Similarly, the maximum and minimum voltage slope (blue rightward and leftward triangles, respectively) were used to compute positive and negative slope thresholds (blue dash-dotted lines, right panel; $0.25 \cdot \max(dV/dt)$ and $0.25 \cdot \min(dV/dt)$, respectively). The active phase, or event, is the portion of the trajectory in the interval beginning with the black square and ending with the black circle, and the silent phase is the complement (circle to square). Local maxima are denoted with red plus symbols

Salient points of trajectories, including active and silent phase transition points, and local maxima and minima of voltage are used to compute a running mean of feature values for each trajectory. These include event period (elapsed time between upward threshold crossings), event amplitude ($\max V - \min V$, per period), event duration (elapsed time between upward and downward threshold crossings), event area (the area between the trajectory and the voltage threshold over the duration of the active phase), and number of local maxima per event (red plus symbols, Fig. 1). For all trajectories, the running mean V is also computed, which represents the resting potential in non-oscillatory trajectories. Only the features are stored for display and analysis, not the full time courses. XPPAUT (Ermentrout 2002) was used to compute bifurcation curves. The computer code for XPPAUT containing all parameter sets of interest is available for download at http://www.math.fsu.edu/~bertram/software/bursting/.

3 The model database

3.1 Generating the database

We consider a model database in which 8192 parameterizations of the model (hereafter referred to as "models") populate a parameter space consisting of ±75 % of the default values of g_{Ca}, g_K, g_{SK}, g_L, and k_C. The extent of this parameter space was chosen so that a non-trivial percentage of models displayed different behaviors of interest, including hyperpolarized and depolarized steady states, spiking, and bursting. To uniformly sample parameter space we used Latin hypercube sampling (McKay et al. 1979). Models are classified based on the features of their numerical solutions. Nonoscillatory models had steady states distributed between -70 and +20 mV, but, interestingly, very few models had membrane potential in the -30 to -20 mV range (Fig. 2a). Because of this clear separation we classified the nonoscillatory models as "depolarized" if their resting potential was above -30 mV, and as "hyperpolarized" otherwise. For oscillatory models, the number of local maxima per event was a

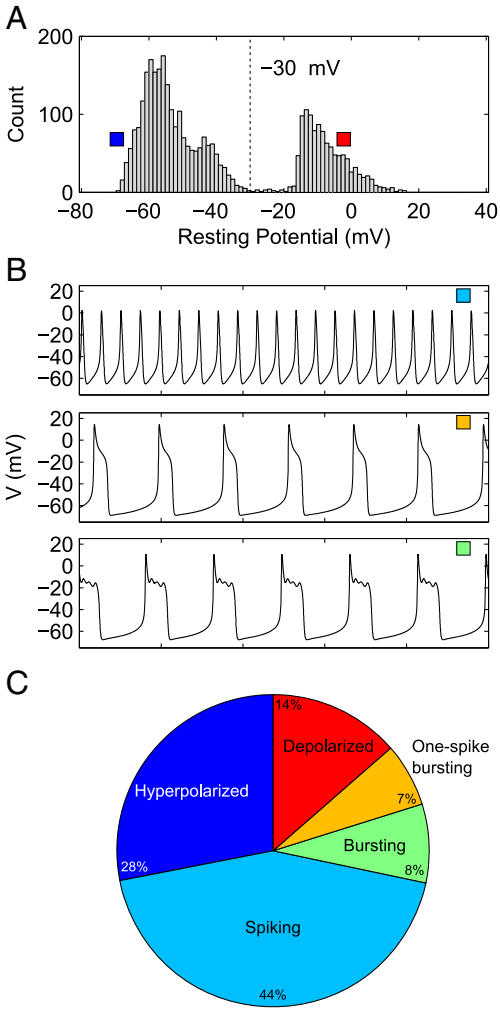

Fig. 2 Classification of models. The 8192 models were generated by Latin Hypercube sampling of a 5-dimensional parameter space constructed as ±75 % of the default parameter set. **a** Silent models are classified as hyperpolarized or depolarized if the resting potential is below or above -30 mV, respectively. **b** Representative trajectories for the spiking (*top panel*), one-spike bursting (*middle panel*), and bursting (*bottom panel*) classes. The voltage trace is computed using the model with the mean parameter values of all models for each class. **c** Percentages of the 8192 models represented by each class

Author's personal copy

key feature used in classification. Models showing one peak per event could be divided into two groups; models with events of area larger than 3 $mV \cdot s$ and amplitude $>$ 30 mV were classified as one-spike bursting (Fig. 2b, middle). The remaining models were considered to be spiking (Fig. 2b, top). Models with events that had more than one peak per event were classified as bursting (Fig. 2b, bottom). The percentages of each class of model in the parameter space examined are shown in Fig. 2c.

3.2 Properties of the database subpopulations

We show in Fig. 3 how the models in each class cluster in projections into a 3-dimensional subspace. For hyperpolarized models (Fig. 3a), we project into the (g_{Ca}, g_{SK}, k_C) subspace. This shows that hyperpolarized models tend to occur for parameter values where k_C is relatively low. This is explained below in terms of the c-nullcline, the curve $dc/dt = 0$. The remaining model classes show distinct localization in the (g_{Ca}, g_K, g_{SK}) subspace. Spiking models (Fig. 3b) occupy the majority of parameter space, while bursting models (Fig. 3c) and one-spike bursting models (Fig. 3d) form a somewhat planar region separating spiking models from depolarized models (Fig. 3e). Bursting models tend to have higher g_K values than one-spike bursting models, while the latter tend to have higher g_{SK}. Depolarized models tend to have low values of both g_K and g_{SK} with simultaneously high g_{Ca}. The collection of all spiking, bursting, and depolarized models are shown in Fig. 3f.

We now examine the behavior of a representative model for each class using fast-slow analysis (Rinzel and Ermentrout 1998). We consider as representative the models given by the mean parameter values of each class, since in each case those models display the correct behavior for its class. The slowest variable c is treated as a bifurcation parameter, yielding a subsystem of the remaining fast variables (the fast subsystem). A bifurcation diagram is then created which shows the solutions present in the fast subsystem as a function of c (Fig. 4a–e). In the case of the mean hyperpolarized model (Fig. 4a), for example, the fast subsystem has a depolarized stable equilibrium for low values of c, which loses stability at a subcritical Hopf bifurcation. This gives rise to a branch of periodic spiking solutions, which continues until its termination at $c \approx 0.2$ μM at a saddle-node on invariant circle (SNIC) bifurcation. For larger c values the fast subsystem again has a stable equilibrium, which is now at a hyperpolarized voltage. The z-shaped curve of stationary solutions is often called the "Z-curve".

Superimposing the curve $dc/dt = 0$ (the c nullcline, orange dash-dotted curve) on this diagram divides the plane into regions of $dc/dt > 0$ and $dc/dt < 0$ (above and below the nullcline in Fig. 4, respectively). The intersection of the

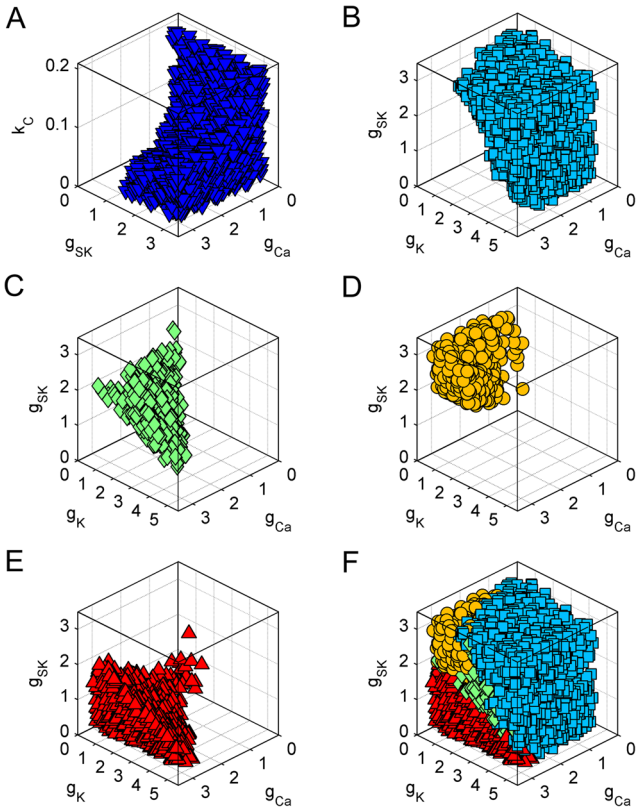

Fig. 3 Parameter values of models of each class projected into 3-dimensional subspaces of parameter space. **a** Hyperpolarized model parameters projected into the (g_{Ca}, g_{SK}, k_C) subspace. Spiking **b**, bursting **c**, one-spike bursting **d**, and depolarized **e** models are located in non-overlapping clusters **f** when projected into the (g_{Ca}, g_K, g_{SK}) subspace. The conductance parameters have units of nS and k_C has units of ms^{-1}

c nullcline and the Z-curve is an equilibrium point of the full system. Indeed, how the c nullcline intersects the Z-curve determines the behavior of the full system (full system trajectories are plotted in blue in Fig. 4). In the case of the hyperpolarized model, the c nullcline intersects the lower branch of stable steady states, so the full system is at a stable hyperpolarized steady state (Fig. 4a, blue point).

The mean spiking model (Fig. 4b) differs mainly in that the c nullcline is higher and intersects the Z-curve in the middle branch. Since this branch is unstable, the full system equilibrium is unstable. However, the intersection with the stable periodic branch leads to a periodic spiking solution of the full system. In the figure, the trajectory moves with a clockwise orientation. In the mean bursting model (Fig. 4c) the Hopf bifurcation is moved to the right, creating a region of bistability between the low and high stationary branches for intermediate c values. The stable periodic branch has been annihilated, and the unstable periodic branch now terminates at a homoclinic bifurcation on the middle branch of the Z-curve, as is characteristic of pseudo-plateau type

Author's personal copy

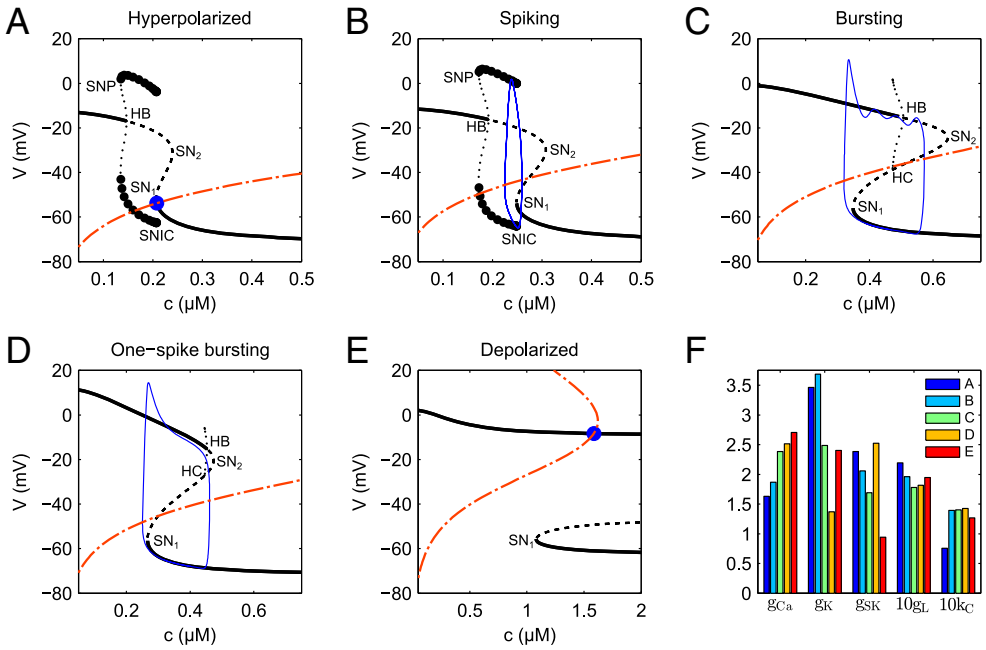

Fig. 4 Fast-slow analysis of the mean model of each class. **a-e** Fast subsystem bifurcation diagrams (*black*) for the mean model of each class, showing the stable and unstable steady states (solid and dashed curves), and stable and unstable periodic orbits (large and small dots). Superimposed are the c-nullcline (orange dash-dotted) and a trajectory of the full system *(blue)*. HB - Hopf bifurcation; SN - Saddle node bifurcation; SNP - Saddle node of periodic orbits; HC - Homoclinic bifurcation; SNIC - Saddle node on invariant circle. **f** Comparison of the parameter values of each of the mean models. The conductance parameters have units of nS and k_C has units of ms^{-1}

bursting (Stern et al. 2008; Teka et al. 2011b; Osinga et al. 2012). The mean one-spike bursting model (Fig. 4d) is similar, with the Hopf bifurcation even closer to the second saddle-node bifurcation (SN_2). Finally, in the mean depolarized model (Fig. 4e) the upper and lower branches have become disconnected and the c nullcline now intersects the upper branch of stable steady states, so the full-system equilibrium is stable at a depolarized voltage.

The fast/slow decomposition of the full model used here is insufficient to understand why there are small oscillations ("spikes") in the bursting case and not in the one-spike bursting case. The distinction between these two cases is best understood using a fast/slow analysis in which two of the variables are considered slow (n and c). Detailed analysis has shown that the bursting is due to a folded node singularity, and the number of small oscillations in the burst depends on the eigenvalues of the folded node and on where the trajectory enters the so-called "singular funnel" (Teka et al. 2011a; Vo et al. 2013, 2014). Although the fast/slow analysis shown in Fig. 4 is unable to distinguish bursting from one-spike bursting, it is sufficient to distinguish both classes of bursting from the other behaviors.

The parameter values for the mean models of each class are summarized in Fig. 4f. g_{Ca} increases monotonically in panels A-E, while the profiles of other parameters vary. Parameter values for hyperpolarized and spiking models are mostly similar, with high values of g_K promoting the presence of the stable periodic branch of the fast subsystem. They differ in terms of the height of the c nullcline, controlled by k_C (low for the hyperpolarized model, higher for the spiking model). g_{SK} declines monotonically through panels A-E, except for the one-spike bursting model, which exhibits low g_K and high g_{SK}. Finally, the low value of g_{SK} and high value of g_{Ca} in the depolarized model underlie the extended stability of the upper branch as well as the movement of SN_1 to far higher c values, promoting the intersection of the c nullcline with the upper branch of stable steady states.

4 The effects of increasing potassium conductances in the model database

4.1 Changes in model subpopulations

It is biologically important to know the effects of various ionic conductances on the cell's electrical activity. However, the effect of adding a conductance may depend greatly on the context, i.e., the values of other parameters. In fact, it may not even be possible to identify a general effect. We investigate this now, focusing on three conductances that are often regulated by hormones in pituitary cells (Stojilković et al. 2010). To each model in the database we independently add each of the three potassium conductances, g_{Kir}, g_A, and g_{BK}. For each of these conductances, we simulate 21 increments evenly spaced over the ranges of $g_{Kir} \in [0, 2]$ nS, $g_A \in [0, 100]$ nS, and $g_{BK} \in [0, 4]$ nS. At each increment, the entire model database is re-classified based on the new activity features. The net changes in each subpopulation as a function of K^+ conductances are depicted in Fig. 5, with the percentages along the y-axis ($g_{Kir} = g_A = g_{BK} = 0$) equal to those shown in Fig. 2c. The changes due to g_{Kir} (left panel) and g_A (center

Author's personal copy

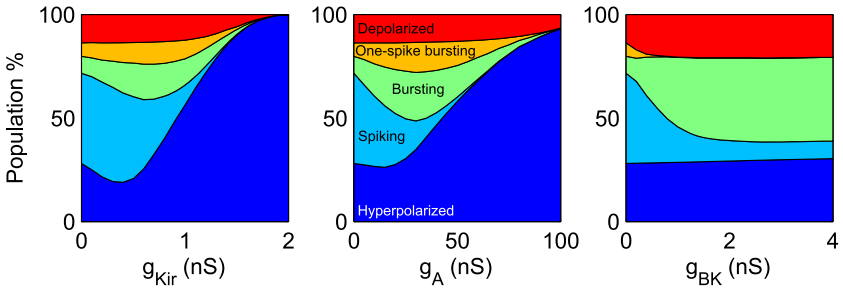

Fig. 5 Adding K^+ conductances cause transitions between classes and changes in model subpopulation sizes. Increasing values of each of g_{Kir} (*left*), g_A (center), and g_{BK} (*right*) were added to each model in the database and the database reclassified

panel) are similar. Initially there is a decline in the number of hyperpolarized models, while bursting models of both types increase in numbers. The spiking model population increases slightly before an ultimate decline in the case of adding g_{Kir}, while it declines monotonically when g_A is added. There is a gradual decline in numbers of depolarized models, and eventually models of all classes become hyperpolarized. This is expected since both of these currents can be active at hyperpolarized potentials, and both tend to further hyperpolarize the cell. The g_{BK}-induced changes differ significantly (Fig. 5, right panel). There is no change in the numbers of hyperpolarized models, which is expected since the BK current requires depolarization for activation. The spiking population declines to a fraction of its initial percentage, and the one-spike bursting population disappears as g_{BK} is increased. The bursting and depolarized populations increase and all populations end up at a stable level for high values of g_{BK}.

The changes in size of each model population gives a "macroscopic view" of the effect of each K^+ conductance on electrical activity, but does not offer insight as to which transitions between model classes are actually occurring in individual models. To get this "microscopic view", we next examine the first K^+ conductance-induced transition for each model in the database. Figure 6a shows the location of the initially hyperpolarized (blue downward triangles, left), spiking (pale blue squares, center), and bursting (green diamonds, right) models in 3-dimensional parameter subspaces, as in Fig. 3. The first transition, if any, due to adding g_{Kir} (Fig. 6b), g_A (Fig. 6c), or g_{BK} (Fig. 6d) was then determined. The models' parameter values are then depicted by the marker and color of the model class after this first transition, or by the original class marker if no transition occurred at any conductance value. For example, when g_{Kir} is added to the population of hyperpolarized cells, many stay hyperpolarized. However, some become spiking cells (light blue, Fig. 6b left) and a few become one-spike bursters (yellow, Fig. 6b left). These are just first transitions; for sufficiently large g_{Kir} all cells become hyperpolarized (Fig. 5).

As was seen in Fig. 5, the effects of g_{Kir} and g_A are similar (Fig. 6b,c). It is unexpected to see that a significant fraction of hyperpolarized models are converted to spiking (left panels). In the case of initially spiking models, all models are converted to another class (center panels). The majority of spiking models transition to bursting, while the remaining subset transition to one-spike bursting (orange circles) or hyperpolarized steady states. Bursting models are again entirely converted to other model classes, this time split roughly evenly between one-spike bursting and hyperpolarized (right panels). The effects of g_{BK} are quite different (Fig. 6d). Hyperpolarized models are unaffected by g_{BK}, and remain quiescent. Spiking models largely become bursting, while a small subset become depolarized (red upward triangles) and some remain spiking for all values of g_{BK} tested. Many of the bursting models remain bursting when g_{BK} is increased, but a subset become depolarized. There are a small number of models that show other transitions, but due to their scarcity they will not be discussed.

A summary of all the first transitions induced by the K^+ conductances is presented in Fig. 7 as a first-transition matrix. The initial, unstimulated model class (with $g_{Kir} = g_A = g_{BK} = 0$) is presented as the row label of the matrix. The class of the model after its first transition is depicted as the column label of the matrix. The diagonal entries of the matrix represent the fraction of models whose class was unchanged by the addition of a K^+ conductance. The $(i, j)^{\text{th}}$ entry of the matrix represents the fraction of models, initially of class i, that transition to another class, given by column j. Thus, the transition matrix tracks the fate of all models in the database as g_{Kir} (left), g_A (center), or g_{BK} (right) are increased, up to the first transition that was induced. These matrices offer a signature of the effect of each K^+ conductance across the whole database of models. They clearly show the similarities between g_{Kir} and g_A, and the distinct profile of g_{BK}-induced transitions previously described in Figs. 5 and 6.

The major transitions depicted in Fig. 7 are, for g_{Kir} and g_A, hyperpolarized to spiking, spiking to bursting, bursting

Author's personal copy

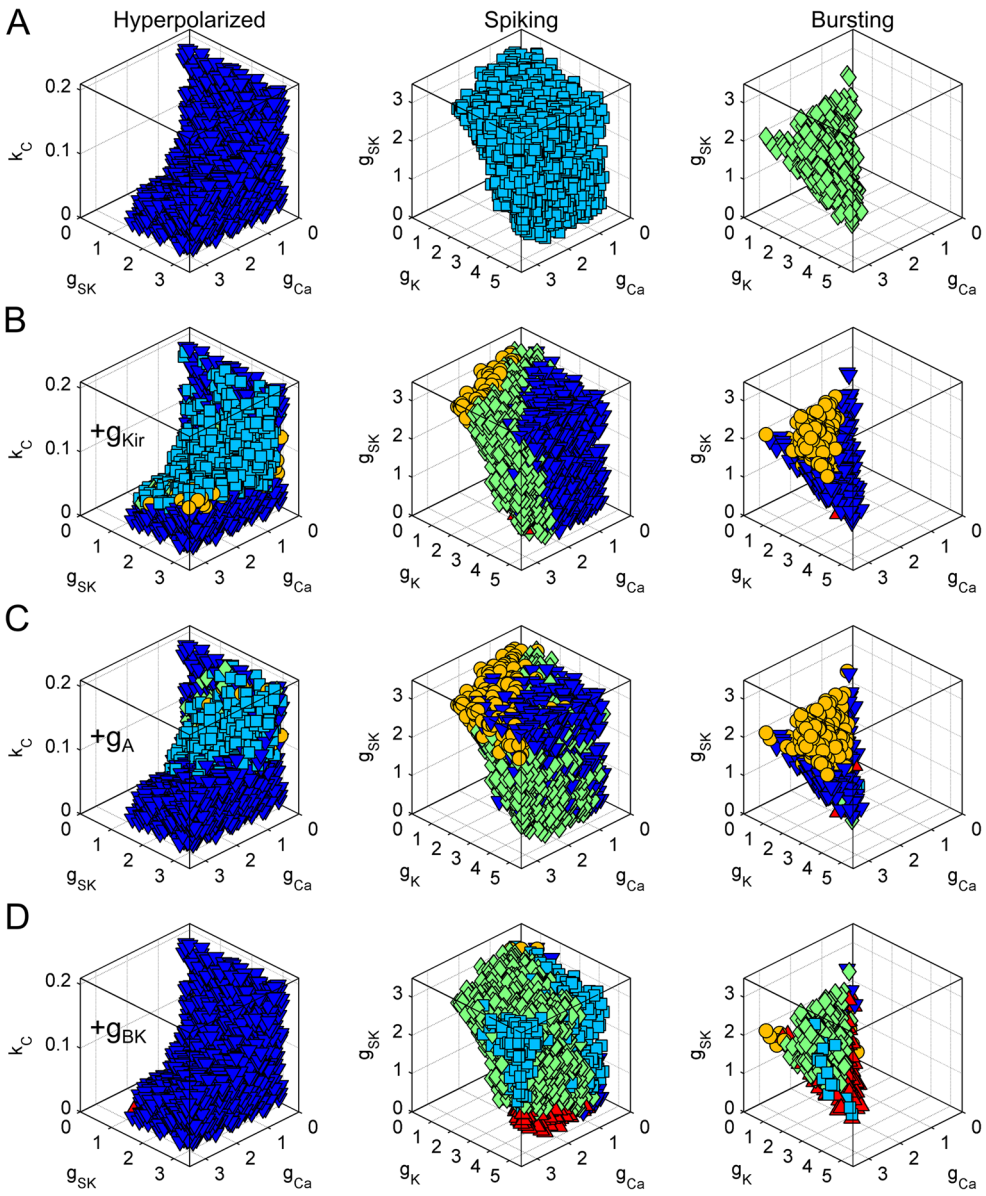

Fig. 6 Model class following the first transition induced by adding a K^+ conductance. **a** The sets of parameter values initially associated with the hyperpolarized (*left*), spiking (center) and bursting models (*right*). **b-d** The same set of models, now showing the class of the model after the first transition (if any) induced by g_{Kir}, g_A, and g_{BK}, respectively. Blue downward triangles - hyperpolarized; pale blue squares - spiking; green diamonds - bursting; orange circles - one-spike bursting; red upward triangles - depolarized

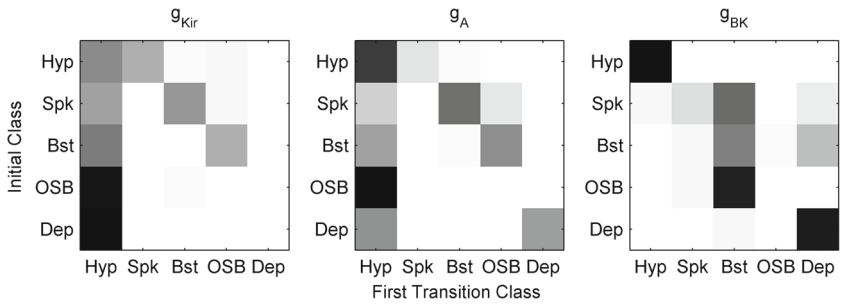

Fig. 7 Summary of all first transitions induced by increasing g_{Kir} (*left*), g_A (center), or g_{BK} (*right*). The initial, unstimulated model class is presented as the row label of the matrix. The class of the model after its first transition is depicted as the column label of the matrix. Those models whose class remains unchanged across all values of added conductance are represented by the diagonal elements of the matrices. Values in each row sum to 1, accounting for the fate of all members of each initial class. Hyp - Hyperpolarized, Spk - Spiking, Bst - Bursting, OSB - One-spike bursting, Dep - Depolarized

Author's personal copy

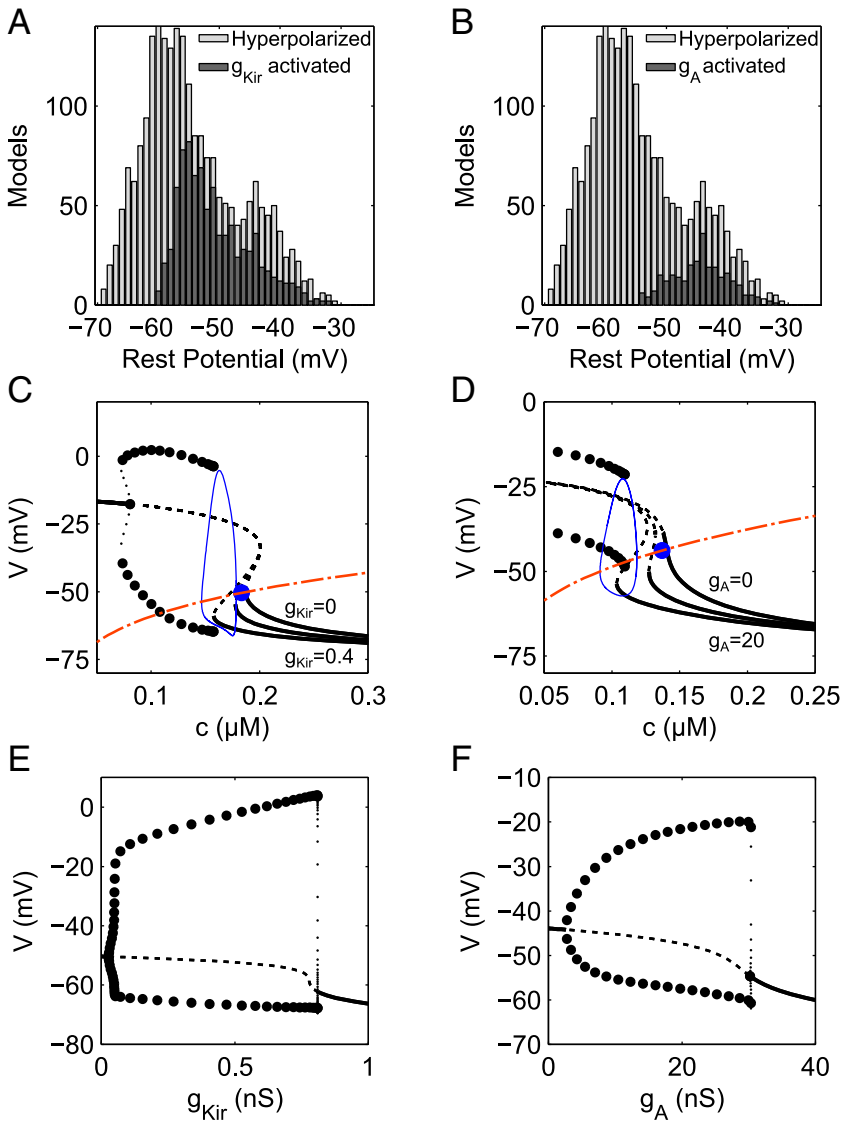

Fig. 8 Hyperpolarized cells with somewhat high resting potential can be activated by g_{Kir} or g_A. **a** Increasing g_{Kir} induces spiking in 39.5 % of hyperpolarized models. **b** Increasing g_A induces spiking in 14.1 % of hyperpolarized models. **c** Fast-slow analysis is used to show the mechanism, using the model with mean parameter values of the subset of models showing g_{Kir}-induced spiking as a representative example. The meaning of all curves is the same as in Fig. 4. The low saddle-node moves down and left, so the crossing point of the c nullcline and the Z-curve moves from the lower branch (blue point, $g_{Kir} = 0$) to the middle branch. For clarity, only the periodic branch for $g_{Kir} = 0.4$ is shown. **d** Fast-slow analysis of the model with mean parameter values of the subset of models showing g_A-induced spiking as a representative example, showing a similar mechanism to g_{Kir}. **e, f** Full-system bifurcation diagrams show that spiking arises due to a supercritical Hopf bifurcation in the full system upon increasing g_{Kir} and g_A, respectively

to one-spike bursting, and from all classes to hyperpolarized. For g_{BK}, the most prominent transitions are spiking to bursting, bursting to depolarized, and one-spike bursting to bursting. We next use bifurcation and fast/slow analysis to understand some of these main transitions.

4.2 Inward rectifier and A-type conductances can activate hyperpolarized models

The first counterintuitive transition considered is that adding hyperpolarizing currents g_{Kir} and g_A converts a subset of hyperpolarized models to a spiking pattern (Fig. 8). Figure. 8a,b shows, at each resting potential, the number of models activated by g_{Kir} or g_A (black bars) and the number that remain hyperpolarized regardless of the amount of added conductance. Those that are activated by the conductance tend to have somewhat depolarized resting potentials.

To understand the mechanism for this effect, we consider the model with mean parameter values across the subset of hyperpolarized models activated by g_{Kir} or g_A as representative models. Fast/slow analysis shows that when $g_{Kir} = 0$ (Fig. 8c) the c nullcline intersects the stable hyperpolarized branch of the Z-curve, leading to a hyperpolarized steady state (blue point). As g_{Kir} is increased, the lower saddle-node point moves down and to the left, so that the c nullcline intersects the unstable middle branch of the Z-curve and the stable spiking branch, so periodic spiking occurs (blue loop, $g_{Kir} = 0.4$). A similar situation occurs for the mean g_A-activated model (Fig. 8d). In this case, for $g_A = 0$, there are no saddle-node points on the "Z"-curve, but the c nullcline still intersects at a hyperpolarized stable steady state. Increasing g_A leads to the appearance of

Author's personal copy

the low and high saddle-node points through a cusp bifurcation, and the lower saddle-node moves down and left as with g_{Kir}. It is clear from these two panels that if either g_{Kir} or g_A are increased enough, the lower saddle node will pass beyond the c nullcline, resulting in a transition to a hyperpolarized steady state. Indeed, this is the mechanism for how sufficient levels of these two current cause hyperpolarization in all model classes. A bifurcation analysis of the full system demonstrates that increasing both conductances leads to the loss of stability of the hyperpolarized steady state via a supercritical Hopf bifurcation (Fig. 8e, f). As the conductances are further increased, the periodic orbit loses stability at a saddle-node of periodic orbits, and the hyperpolarized steady-state regains stability via a subcritical Hopf bifurcation.

Two subpopulations of models are not activated by g_{Kir} (light grey bars, Fig. 8a). The more hyperpolarized group is characterized by low values of k_C, leading to the crossing of the c-nullcline with the hyperpolarized branch of steady states, as in Fig. 4a. The other subpopulation is characterized by low values of g_{Ca} and a complete lack of a periodic solutions in the upper branch of the Z-curve.

4.3 Potassium conductances promote bursting in spiking models

One of the main effects seen in the first-transition matrix is that adding K^+ channels converts spiking models to a bursting pattern. This effect has been studied in great detail for g_A and g_{BK} using a similar system with parameters similar to the default model parameters in Table 1 (Tabak et al. 2007; Teka et al. 2011a; Toporikova et al. 2008; Vo et al. 2010, 2014). Here, we observed this transition in 50.5 % of spiking models when g_{Kir} was increased, 64.4 % for g_A, and 68.5 % for g_{BK}. For fast/slow analysis, we consider here as representative example models the mean of the subset of spiking models that are converted to bursting by g_{Kir}, g_A, and g_{BK} (Fig. 9a, c, e, respectively). When all three K^+ conductances are zero (square marker in Fig. 9a c and e), we have a situation similar to the mean spiking model. There is a stable periodic branch, and the c nullcline intersects the middle branch of the Z-curve giving rise to spiking oscillations in the full model (the periodic branch is omitted for clarity). When either g_{Kir} or g_A are increased, the lower saddle-node point moves to the left and down (circle and diamond in Fig. 9a, c). The stable branch of periodic orbits vanishes, and a region of bistability increases toward low c values. The result is a picture that is characteristic of pseudo-plateau bursting (Stern et al. 2008). In the case of g_{BK} (Fig. 9e), the main effect is that the Hopf bifurcation and associated branch of periodic orbits are moved to the right. The interval of bistability again increases, but this time toward higher c values. This analysis predicts that adding g_{Kir} or g_A will result in a decrease in calcium entry due to the creation of a bistable region to the left, while adding g_{BK} should increase calcium entry.

The transition from spiking to pseudo-plateau bursting with changes in K^+ conductance has been analyzed previously in great detail using fast/slow analysis and bifurcation analysis of full systems similar to the one presented here. In a 4-variable pituitary cell model, (Vo et al. 2013) found that the transition from spiking to pseudo-plateau bursting in the full system was similar for g_K, g_{BK}, and g_A, and involved the loss of stability of the spiking solution via a period doubling bifurcation. A later study re-examined the g_{BK}-induced transition, but this time taking into consideration the rate of activation of the BK channel (Vo et al. 2014). These results were obtained for a fixed context of the other model parameters. Another detailed study using fast/slow analysis and full system bifurcation analysis, using a modified Hindmarsh-Rose model (Hindmarsh and Rose 1984), has been used to show how the unstable full-system equilibrium affects the number of spikes in a burst (Osinga and Tsaneva-Atanasova 2010; Tsaneva-Atanasova et al. 2010). Those studies showed similarities between the spike adding bifurcations present in pseudo-plateau and those occurring in plateau bursting, which were analyzed in detail earlier (Terman 1992).

In the full system, we can rapidly compute the features of solutions in a two parameter plane near each of the representative models using the GPU (Fig. 9b, d, f). Here we show how the number of peaks per event changes with each K^+ conductance and k_C, which shifts the c nullcline vertically. For low k_C, each of the three models shows a region of hyperpolarized steady states (white region), separated from the oscillatory domain (gray shaded region) by a curve of Hopf bifurcations (not shown, but approximated by the contour separating hyperpolarized and oscillatory models in the plane). In panels B and D, there is a small window of k_C values for which adding g_{Kir} and g_A, respectively, convert the model from hyperpolarized to spiking. Once above some minimal k_C value, bursting can be induced by a sufficient increase in K^+ conductance in all three cases. As k_C is increased, the bursting interval becomes wider, which is expected since this brings the c nullcline nearer to the top branch of solutions in the fast subsystem.

5 Discussion

In this study, we used a combination of a global sampling of parameter space and local analysis of representative parameter sets to understand the effects of adding ionic currents to a population of pituitary cell models. The global sampling, or model database, ensured that we capture a wide

Author's personal copy

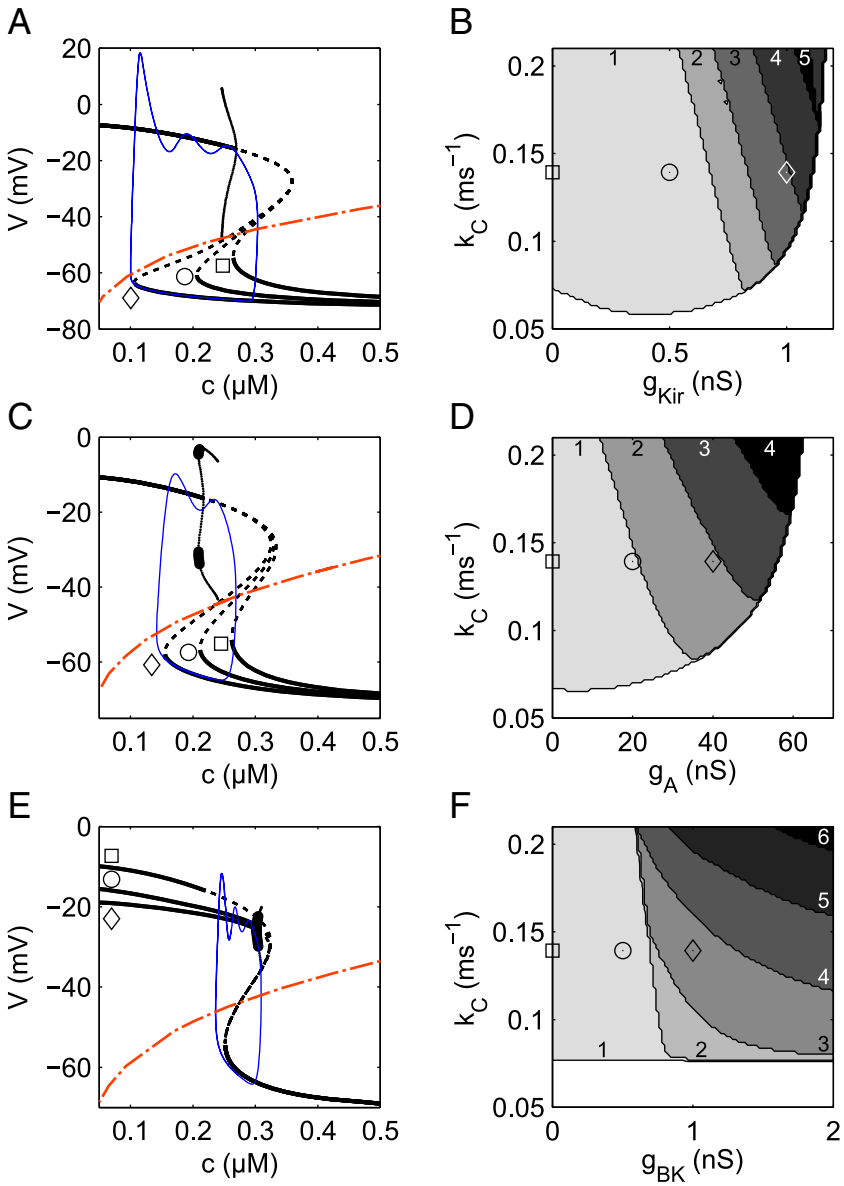

Fig. 9 Increasing g_{Kir}, g_A, and g_{BK} can convert spiking to bursting. **a**, **c**, **e**. Effects of increasing g_{Kir}, g_A, and g_{BK} on the fast subsystem equilibria, respectively. The meaning of all curves is the same as in Fig. 4. In each case, the mean model of that subset is used as a representative parameter set. For clarity, the periodic branch and full system trajectories of only the highest value of added K^+ are shown (diamonds). **b**, **d**, **f** Peaks per event in the full model as a function of k_C and each of g_{Kir}, g_A, and g_{BK}, respectively. The white regions represent hyperpolarized steady states, while the gray shaded regions represent solutions with one or more peaks per event, indicated by numbers. Square, circle, and diamond markers in the right panels correspond to the parameter combinations used to generate the bifurcation diagrams in the left panels. Each two-parameter plane consists of contour plots generated from a grid of 96x96 parameter combinations, run to a final simulation time of 30 s, which required a computation time of 7 s on a laptop with an nVidia GeForce GTX 870M

variety of contexts of model parameters from which to evaluate the effects of introducing K^+ conductances. We classified the models in the database according to their activity patterns, and determined how the proportions of these classes changed with increasing K^+ conductances. Furthermore, we identified the first transition between activity classes for each model, summarized as the first-transition matrix. Together with the net changes in activity-class proportions, this first-transition matrix is a signature of *what* changes occur due to each potassium conductance. We then identified the subpopulations of models that underwent specific (and sometimes unexpected) transitions between activity patterns. Finally, we used bifurcation analysis and fast/slow analysis to investigate *why* those transitions occur in representative individual models. Combining these two approaches therefore allows us to predict the effects of addition of an ionic conductance, depending on the context of other cell parameters to which the conductance is added, and allows us to understand the mechanism underlying these effects.

Using this combined approach we uncovered the counterintuitive finding that adding the hyperpolarizing conductances g_{Kir} or g_A could cause silent models to begin to spike continuously. It seems unlikely that we would have found this transition without using the global parameter search we performed. It should be noted that adding an ohmic hyperpolarizing current or negative current injection would also trigger this transition, by the same mechanism. Furthermore, this transition could also occur in reverse when recording from pituitary cells; a depolarizing leak conductance due

Author's personal copy

to a non-ideal seal might be sufficient to silence a spiking cell. We also found that the conversion of spiking models to bursting due to g_{Kir}, g_A, and g_{BK} is a robust effect, as it occurred in the majority of spiking models in the database. Furthermore, the switch to bursting due to g_{Kir} or g_A is unlikely to lead to increases in calcium entry, since fast/slow analysis presented here and elsewhere (Tabak et al. 2007) showed that bursting arises due to movement of the low knee of the Z-curve toward lower values of c. Conversely, g_{BK} triggers bursting by increasing a region of bistability in the fast subsystem via rightward movement of a Hopf bifurcation on the top branch of the Z-curve, so that the mean c increases.

The abundance and low cost of modern GPUs as well as the increasing ease of software implementation offers promise for acceleration of a wide range of parameter studies such as the one presented here, with increasing adoption in various fields (Rodríguez et al. 2015; Barrio et al. 2015; Brette and Goodman 2012; DeWoskin et al. 2014). The combined numerical simulation and extraction of features on the GPU makes database and parameter sweep computations, such as the two parameter planes shown in Fig. 9, fast enough that they can be used in a "disposable" way. This allows one to rapidly explore the dependence of features on parameters over much larger regions of parameter space than would otherwise be possible, while maintaining the intuition-building benefits of the "hand-tuning" approach.

The use of the GPU to compute solution features allows for rapid survey of how parameters and initial conditions affect solution features. With random sampling of parameter space, this method will find solutions of a given type with probability proportional to the volume of the region in parameter space for which that qualitative type of behavior occurs. It is unlikely to find special solutions that occur for very limited regions in parameter space. For example, this approach is unsuitable for directly finding the bifurcation manifolds which divide the parameter space into regions of qualitatively distinct behaviors, since these tend to occur as low dimensional subspaces of parameter space. These must be inferred by the presence of two qualitatively different types of solutions in neighboring regions of parameter space. For this reason, "local" techniques such as numerical continuation are invaluable as complementary tools, since they are specifically designed to track bifurcations. Fast/slow analysis can be used to understand the mechanisms underlying the observed solutions at a point in parameter space, and how this mechanism is altered by changing parameters.

The ODEs of a model map a parameter set and initial conditions to a solution trajectory, such that there may be coexistence of stable attractors (multistability) for a single parameter set. Here, we fixed the initial condition for all parameter sets sampled, so regions in parameter space in which there is multistability were not identified. We expect that multistability should occur in some regions of parameter space, and that in general the effect of adding a conductance may depend also on the initial condition in those cases. Random sampling of both parameters and initial conditions leads to a very large number of simulations for even a few parameters, and for the same reasons explained above, it is unlikely to discover solutions for which the basin of attraction (in initial condition space) occupies a small volume in parameter space. These drawbacks highlight the fact that direct brute simulation is likely not the best approach for discovering multistability in model databases. A better approach is to instead use numerical continuation for each member of the database to discover the set of attractors that exist, as was done by (Marin et al. 2013) for a subset of a database of leech heart half-center oscillators (Doloc-Mihu and Calabrese 2011). For the database presented here, we leave the characterization of multistability to future work.

The wide variety of changes that occurred in the model database highlights the challenge of making accurate model predictions in light of cell-to-cell heterogeneity. This motivates the need for understanding how to map heterogeneity in behaviors of a population of cells to regions of parameter space in a putative model for these cells, a task for which the model database approach is well suited. Here we used this approach to demonstrate context dependence of the effects of adding new conductances to a lactotroph model, simulating the effects of stimulation by a hormone. Model database approaches in other studies have yielded findings regarding the robustness or context dependence of conductances. (Goldman et al. 2001) used a database of STG neurons to show that model behavior was robust to parameter changes in some directions in a 5-D conductance space, while sensitive in others, a result with implications for the action of neuromodulators. (Günay et al. 2008) were able to account for most variability in globus pallidus neurons using variability in conductances in a model database, while showing that the role of each conductance could vary depending on the context of other parameters. In a lactotroph model, the robustness of burst-promoting effects of the BK-type potassium conductance was demonstrated using a small database (Tabak et al. 2011), and a robust effect of increasing sodium conductance on the f-I curve of crab STG neurons (increasing frequency at low applied current, while decreasing frequency at high applied current) was demonstrated by (Kispersky et al. 2012). (Caplan et al. 2014) examined how temperature dependence of ion channel kinetics (using databases of Q10 parameters) contributes to temperature robustness of network output of the crab pyloric central pattern generator of the STG. Model database approaches have

Author's personal copy

also been used to answer several other types of biologically motivated questions. These include attempts to find and study the region in parameter space which supports a desired model behavior within some tolerance, yielding an ensemble of models instead of just a single parameter set (Foster et al. 1993; Prinz et al. 2003; Taylor et al. 2009; Caplan et al. 2014). This type of parameter optimization has led to evidence that in some conductance based models, very similar model behaviors have been found to arise from disparate regions in parameter space (Prinz et al. 2004; Günay et al. 2008). Model databases have also been used to study the constraints on parameters that define connectivity between neurons in pattern generating networks, and how these give rise to the appropriate network behavior (Prinz et al. 2004; Calin-Jageman et al. 2007; Doloc-Mihu and Calabrese 2011; Williams et al. 2013).

Combining global parameter space sampling and local analysis to explore the relationship between parameter sets and model behavior holds general promise. In our study, we use the word "model" to refer to a particular parameterization of a specific (fixed) set of differential equations. In that sense, we are interested in mapping out the set of all types of possible solutions to a given ODE model in terms of the model parameters and initial conditions, i.e., the "modelome" generated by those equations. This is a natural first step in the exploration of the properties of a model and how they rely on parameter values, and it is now becoming a feasible task even on desktop and laptop workstations by running simulations on GPUs. Techniques aimed at gaining a global understanding of a particular system of equations are analogous to global approaches appearing in biology today. For example, the field of genomics is concerned with the study of the structure and function of the entire set of genetic information contained in an organism, namely the genome. A similar large-scale global approach is used to study metabolism (metabolomics), protein structure (proteomics), and neuron connectivity (connectomics). The study of the relationships between parameters, initial conditions, and the associated ODE solutions could similarly be called "modelomics." New tools will be needed to explore the large amounts of data generated in order to discover the patterns and relationships that underlie structure and function.

Acknowledgments This work was supported by grant DMS1220063 from the National Science Foundation.

Compliance with Ethical Standards

Conflict of interests The authors declare that they have no conflict of interest.

References

Barrio, R., & Shilnikov, A. (2011). Parameter-sweeping techniques for temporal dynamics of neuronal systems: Case study of hindmarsh-rose model. *The Journal of Mathematical Neuroscience*, *1*(1), 6.

Barrio, R., Rodríguez, M., Serrano, S., & Shilnikov, A. (2015). Mechanism of quasi-periodic lag jitter in bursting rhythms by a neuronal network. *EPL (Europhysics Letters)*, *112*(3), 38,002.

Brette, R., & Goodman, D.F.M. (2012). Simulating spiking neural networks on GPU. *Network: Computation in Neural Systems*, *23*(4), 167–182.

Calin-Jageman, R.J., Tunstall, M.J., Mensh, B.D., Katz, P.S., & Frost, W.N. (2007). Parameter space analysis suggests multi-site plasticity contributes to motor pattern initiation in tritonia. *Journal of Neurophysiology*, *98*(4), 2382–2398.

Caplan, J.S., Williams, A.H., & Marder, E. (2014). Many parameter sets in a multicompartment model oscillator are robust to temperature perturbations. *The Journal of Neuroscience*, *34*(14), 4963–4975.

DeWoskin, D., Geng, W., Stinchcombe, A.R., & Forger, D.B. (2014). It is not the parts, but how they interact that determines the behaviour of circadian rhythms across scales and organisms. *Interface focus*, *4*(3), 20130,076.

Dhooge, A., Govaerts, W., & Kuznetsov, Y.A. (2003). MATCONT: A Matlab package for numerical bifurcation analysis of ODEs. *ACM Transactions on Mathematical Software (TOMS)*, *29*(2), 141–164.

Doedel, E., & Kernevez, J.P. (1986). AUTO, Software For Continuation And Bifurcation Problems In Ordinary Differential Equations. California Institute of Technology.

Doloc-Mihu, A., & Calabrese, R.L. (2011). A database of computational models of a half-center oscillator for analyzing how neuronal parameters influence network activity. *Journal of Biological Physics*, *37*(3), 263–283.

Ermentrout, B. (2002). *Simulating analyzing And Animating Dynamical Systems*. SIAM: A Guide To XPPAUT For Researchers And Students.

Fakler, B., & Adelman, J.P. (2008). Control of KCa channels by calcium nano/microdomains. *Neuron*, *59*(6), 873–881.

Foster, W.R., Ungar, L.H., & Schwaber, J.S. (1993). Significance of conductances in Hodgkin-Huxley models. *Journal of Neurophysiology*, *70*(6), 2502–2518.

Goldman, M.S., Golowasch, J., Marder, E., & Abbott, L.F. (2001). Global structure, robustness, and modulation of neuronal models. *The Journal of Neuroscience*, *21*(14), 5229–5238.

Günay, C. (2014). Neuronal model databases, In Jaeger, D., & Jung, R. (Eds.) (pp. 1-6). New York: Springer. Encyclopedia of Computational Neuroscience.

Günay, C., Edgerton, J.R., & Jaeger, D. (2008). Channel density distributions explain spiking variability in the globus pallidus: a combined physiology and computer simulation database approach. *The Journal of Neuroscience*, *28*(30), 7476–7491.

Hindmarsh, J., & Rose, R. (1984). A model of neuronal bursting using three coupled first order differential equations. *Proceedings of the Royal Society of London B: Biological Sciences*, *221*(1222), 87–102.

Iooss, B., & Lemaître, P. (2015). A review on global sensitivity analysis methods, In Dellino, G., & Meloni, C. (Eds.) (Vol. 59 pp. 101-122). US: springer. Uncertainty management in simulation-optimization of complex systems operations research/computer science interfaces series.

Kispersky, T.J., Caplan, J.S., & Marder, E. (2012). Increase in sodium conductance decreases firing rate and gain in model neurons. *The Journal of Neuroscience*, *32*(32), 10,995–11,004.

Author's personal copy

Linaro, D., Champneys, A., Desroches, M., & Storace, M. (2012). Codimension-two homoclinic bifurcations underlying spike adding in the Hindmarsh–Rose burster. *SIAM Journal on Applied Dynamical Systems*, *11*(3), 939–962.

Marin, B., Barnett, W.H., Doloc-Mihu, A., Calabrese, R.L., & Cymbalyuk, G.S. (2013). High prevalence of multistability of rest states and bursting in a database of a model neuron. *PLoS Computational Biology*, *9*(3), e1002,930.

McKay, M.D., Beckman, R.J., & Conover, W.J. (1979). A comparison of three methods for selecting values of input variables in the analysis of output from a computer code. *Technometrics*, *21*(2), 239–245.

Osinga, H., & Tsaneva-Atanasova, K. (2010). Dynamics of plateau bursting depending on the location of its equilibrium. *Journal of Neuroendocrinology*, *22*(12), 1301–1314.

Osinga, H.M., Sherman, A., & Tsaneva-Atanasova, K. (2012). Cross-currents between biology and mathematics: The codimension of pseudo-plateau bursting. *Discrete and Continuous Dynamical Systems Series A*, *32*(8), 2853–2877.

Prinz, A.A., Billimoria, C.P., & Marder, E. (2003). Alternative to hand-tuning conductance-based models: Construction and analysis of databases of model neurons. *Journal of Neurophysiology*, *90*(6), 3998–4015.

Prinz, A.A., Bucher, D., & Marder, E. (2004). Similar network activity from disparate circuit parameters. *Nature Neuroscience*, *7*(12), 1345–1352.

Rinzel, J., & Ermentrout, G.B. (1998). Analysis of neural excitability and oscillations. *Methods in Neuronal Modeling*, *2*, 251–292.

Rodríguez, M., Blesa, F., & Barrio, R. (2015). OpenCL parallel inte gration of ordinary differential equations: Applications in computational dynamics. *Computer Physics Communications*, *192*, 228–236.

Sherman, A. (2011). Dynamical systems theory in physiology. *The Journal of General Physiology*, *138*(1), 13–19.

Sherman, A., Keizer, J., & Rinzel, J. (1990). Domain model for Ca^{2+}-inactivation of Ca^{2+} channels at low channel density. *Biophysical Journal*, *58*(4), 985–995.

Stern, J.V., Osinga, H.M., LeBeau, A., & Sherman, A. (2008). Resetting behavior in a model of bursting in secretory pituitary cells: Distinguishing plateaus from pseudo-plateaus. *Bulletin of Mathematical Biology*, *70*(1), 68–88.

Stojilković, S.S., Tabak, J., & Bertram, R. (2010). Ion channels and signaling in the pituitary gland. *Endocrine Reviews*, *31*(6), 845–915.

Storace, M., Linaro, D., & de Lange, E. (2008). The Hindmarsh-Rose neuron model: Bifurcation analysis and piecewise-linear approximations. *Chaos: An Interdisciplinary Journal of Nonlinear Science*, *18*(3), 033128.

Tabak, J., Toporikova, N., Freeman, M.E., & Bertram, R. (2007). Low dose of dopamine may stimulate prolactin secretion by increasing fast potassium currents. *Journal of Computational Neuroscience*, *22*(2), 211–222.

Tabak, J., Tomaiuolo, M., Gonzalez-Iglesias, A.E., Milescu, L.S., & Bertram, R. (2011). Fast-activating voltage- and calcium-dependent potassium (BK) conductance promotes bursting in pituitary cells: a dynamic clamp study. *The Journal of Neuroscience*, *31*(46), 16,855–16,863.

Taylor, A.L., Goaillard, J.M., & Marder, E. (2009). How multiple conductances determine electrophysiological properties in a multicompartment model. *The Journal of Neuroscience*, *29*(17), 5573–5586.

Teka, W., Tabak J., Vo, T., Wechselberger, M., & Bertram, R. (2011a). The dynamics underlying pseudo-plateau bursting in a pituitary cell model. *The Journal of Mathematical Neuroscience*, *1*(1), 1–23.

Teka, W., Tsaneva-Atanasova, K., Bertram, R., & Tabak, J. (2011b). From plateau to pseudo-plateau bursting: Making the transition. *Bulletin of Mathematical Biology*, *73*(6), 1292–1311.

Terman, D. (1992). The transition from bursting to continuous spiking in excitable membrane models. *Journal of Nonlinear Science*, *2*(2), 135–182.

Toporikova, N., Tabak, J., Freeman, M.E., & Bertram, R. (2008). A-type K^+ current can act as a trigger for bursting in the absence of a slow variable. *Neural Computation*, *20*(2), 436–451.

Tsaneva-Atanasova, K., Osinga, H.M., Rieß, T., & Sherman, A. (2010). Full system bifurcation analysis of endocrine bursting models. *Journal of Theoretical Biology*, *264*(4), 1133–1146.

Van Goor, F., Zivadinovic, D., Martinez-Fuentes, A.J., & Stojilkovic, S.S. (2001). Dependence of pituitary hormone secretion on the pattern of spontaneus voltage-gated calcium influx: Cell type-specific action potential secretion coupling. *Journal of Biological Chemistry*, *276*(36), 33,840–33,846.

Vo, T., Bertram, R., Tabak, J., & Wechselberger, M. (2010). Mixed mode oscillations as a mechanism for pseudo-plateau bursting. *Journal of Computational Neuroscience*, *28*(3), 443–458.

Vo, T., Bertram, R., & Wechselberger, M. (2013). Multiple geometric viewpoints of mixed mode dynamics associated with pseudo-plateau bursting. *SIAM Journal on Applied Dynamical Systems*, *12*(2), 789–830.

Vo, T., Tabak, J., Bertram, R., & Wechselberger, M. (2014). A geometric understanding of how fast activating potassium channels promote bursting in pituitary cells. *Journal of Computational Neuroscience*, *36*(2), 259–278.

Williams, A.H., Kwiatkowski, M.A., Mortimer, A.L., Marder, E., Zeeman, M.L., & Dickinson, P.S. (2013). Animal-to-animal variability in the phasing of the crustacean cardiac motor pattern: an experimental and computational analysis. *Journal of Neurophysiology*, *109*(10), 2451–2465.